

Snapshot Acquisition of GNSS Signals in Space: a Case Study at Lunar Distances

Original

Snapshot Acquisition of GNSS Signals in Space: a Case Study at Lunar Distances / Nardin, Andrea; Minetto, Alex; Vouch, Oliviero; Mariani, Margherita; Dovis, Fabio. - ELETTRONICO. - (2022), pp. 3603-3617. (Intervento presentato al convegno 35th International Technical Meeting of the Satellite Division of The Institute of Navigation (ION GNSS+ 2022) tenutosi a Denver, Colorado (USA) nel 19-23 September 2022) [10.33012/2022.18477].

Availability:

This version is available at: 11583/2971244 since: 2022-10-25T08:07:31Z

Publisher:

Institute of Navigation

Published

DOI:10.33012/2022.18477

Terms of use:

This article is made available under terms and conditions as specified in the corresponding bibliographic description in the repository

Publisher copyright

(Article begins on next page)

Snapshot Acquisition of GNSS Signals in Space: a Case Study at Lunar Distances

Andrea Nardin, Alex Minetto, Oliviero Vouch, Margherita Mariani, Fabio Dovis
Department of Electronics and Telecommunications (DET), Politecnico di Torino (Turin, Italy)

BIOGRAPHY

Andrea Nardin received the M.Sc. degree in telecommunications engineering with a thesis on cooperative GNSS ranging integration in positioning algorithms in 2018 from Politecnico di Torino, Turin, Italy, where he is currently a Ph.D. candidate in electrical, electronics and communications engineering with the Department of Electronics and Telecommunications. From 2018, he has been working with the Navigation Signal Analysis and Simulation (NavSAS) group at Politecnico di Torino and in 2021 he was a Visiting Doctoral Researcher at Northeastern University, Boston, MA, USA with the Information Processing Laboratory. His research interests include innovative signal processing architectures and signal design for GNSSs and LEO PNT.

Alex Minetto received the B.Sc. and M.sc. degrees in Telecommunications Engineering from Politecnico di Torino, Turin, Italy and his Ph.D. degree in Electrical, Electronics and Communications Engineering, in 2020. He joined the Department of Electronics and Telecommunications of Politecnico di Torino in 2019 as research and teaching assistant. In 2015 he spent a six-month internship at European Organisation for the Exploitation of Meteorological Satellites (EUMETSAT), Darmstadt, Germany. His current research interests cover signal processing and advanced Bayesian estimation applied to Global Navigation Satellite System (GNSS) cooperative receivers.

Oliviero Vouch received the B.Sc. degree in Electronics and Communications Engineering (ECE) in 2018 and the M.Sc. degree in Communications and Computer Networks Engineering (CCNE) in 2020, both from Politecnico di Torino, Turin, Italy. He joined the Department of Electronics and Telecommunications (DET) of Politecnico di Torino as a PhD student in 2021 and he is member of the Navigation Signal Analysis and Simulation (NavSAS) research group. His academic background includes advanced signal processing and his current research interests cover advanced Bayesian estimation applied to navigation sensors integration.

Margherita Mariani received the M.Sc. degree in Communications and Computer Networks engineering in 2021 from Politecnico di Torino, Turin, Italy, with a thesis on the study of high sensitivity GNSS receivers for space applications and lunar missions, carried out with the Navigation Signal Analysis and Simulation (NavSAS) group. She is currently working as a Wireless Software Engineer at MediaTek, Cambourne, Cambridge, UK, focusing on 5G NR physical layer.

Fabio Dovis received the M.Sc. degree in electronics engineering and Ph.D. degree in electronics and communications engineering from Politecnico di Torino, Turin, Italy, in 1996 and 2000, respectively. He was with the Department of Electronics and Telecommunications, Politecnico di Torino, as an Assistant Professor in 2004 and since 2014, he has been Associate Professor with the Department of Electronics and Telecommunications, Politecnico di Torino, where he coordinates the Navigation Signal Analysis and Simulation research group. He has a relevant experience in European projects in satellite navigation as well as cooperation with industries and research institutions. His research interests include the design of GPS and Galileo receivers and advanced signal processing for interference and multipath detection and mitigation, as well as ionospheric monitoring. Prof. Dovis is a member of the IEEE Aerospace And Electronics Systems Society Navigation Systems Panel.

ABSTRACT

Observation and characterization of GNSS signals in space are gaining momentum for the re-use of GNSS and its integration in Orbit Determination and Time Synchronization solutions, oriented towards more autonomous Guidance, Navigation, and Control systems. In the initial phase of this transient, Radio-Frequency signals observations from space-borne receivers allow supporting GNSS-based space navigation thanks the remote post-processing. This contributes to understand and compensate for unmodelled features of GNSS signals propagating at large distances, up to the Moon's surface. Such activities require the capture of Intermediate Frequency (IF) signal samples, and upcoming Lunar missions, such as the NASA/ASI Lunar GNSS Receiver Experiment (LuGRE) scientific payload, are going to support the collection of raw GNSS signal samples and the transmission of such data to the mission ground segment. The size of such data is the main bottleneck for the typical, narrowband communication channels dedicated to such payloads. Therefore a sufficient amount of signal samples must be defined for an effective post-processing at the ground segment. As an early investigation, this work sets as a minimum objective the acquisition of GPS signals at the low carrier-to-noise density ratio (C/N_0) throughout a sample Moon Transfer Orbit (MTO).

The designed acquisition stage implements high-sensitivity techniques and Doppler compensation to guarantee successful signal acquisition at critical C/N_0 values. By investigating the main acquisition parameters, the proposed study identifies minimum chunks length to be imposed as mission requirements.

I. INTRODUCTION

Global Navigation Satellite Systems (GNSSs) provide accurate Positioning, Navigation and Timing (PNT) capabilities to terrestrial users at a global scale in a plethora of applications (Teunissen and Montenbruck, 2017). Although GNSS constellations were originally designed to serve terrestrial users, continuous and dependable PNT has become an established expectation for space users within the Terrestrial Service Volume (TSV) (i.e., the regime from the surface of the Earth to 3,000 kilometers altitude, including much of low Earth orbit (LEO)) and the interest in the use of GNSS as a navigation system for space missions is recently gaining momentum (Farahmand et al., 2015; Capuano et al., 2015; Winternitz et al., 2009; Montenbruck et al., 2008; Gill et al., 2001; Rush, 2000). Since the early steps of space exploration, missions have been leveraging Orbit Determination and Time Synchronization (ODTS) and Precise Orbit Determination (POD) solutions (Vetter, 2007; Amir et al., 2021), which is the process of accurately estimating and tracking both the position and velocity of the spacecraft along its orbit. This method usually relies on long-term post-processing, based on range and Doppler tracking services offered by federated networks, e.g., National Aeronautics and Space Administration (NASA) Deep Space Network (DSN), and the European Space Tracking Network (ESTRACK), and managed at the ground segment (Lannes, 2011). On the contrary, exploiting real-time, in-orbit GNSS-based navigation systems would make spacecraft more autonomous, thus reducing costs and efforts for ground operations (United Nations (UN), 2018; Parker et al., 2018). Over the past years, the use of in-orbit GNSS receivers has been experimentally confirmed within the Space Service Volume (SSV), as in Low-Earth Orbit (LEO), and up to Geostationary-Earth Orbit (GEO) altitudes. The first spaceborne GNSS receiver, GPSPAC, was deployed in Landsat 4 on July 16th, 1982, and it proved the feasibility of using Global Positioning System (GPS) for space applications at LEO (Montenbruck et al., 2008). Latest missions, then, have unveiled GNSS performance up to distances of about 150 000 km away from the Earth's surface (Hartrampf et al., 2015). NASA's Magnetospheric Multiscale (MMS) has recently shown the feasibility of tracking GPS signals up to this distance (Burch et al., 2016). Hence, high-altitude spacecraft navigation is growing interest and an assessment of PNT capabilities supported by GNSS constellations is of great concern, especially for the upcoming lunar missions (ISECG, 2018; Miller, 2018).

In such framework, GNSS could support spacecraft navigation at Moon distances, thus enabling pioneering experiments about satellite-based positioning in the lunar environment (Capuano et al., 2015; Delépaut et al., 2022). Moreover, this would pave the way to the installation of a permanent space station in lunar orbit and future colonization of the Moon and then, of Mars (ISECG, 2018). However, GNSS receiver deployment at lunar distances is a challenging task due to multiple factors. First, received satellite signals are characterized by low power levels. Moreover, in these conditions the signals transmitted by the main antenna lobes might suffer occultation effects, being received from satellites orbiting on the opposite side of the Earth (Winternitz et al., 2009). Side lobes, on the other hand, only supply low-power signals in the spacecraft direction. Furthermore, they suffer for a higher directivity that may reduce the probability for the receiving antenna of intercepting the radiation pattern in case of mispointing. Besides, signal availability can be drastically impaired by poor geometry conditions, leading to accuracy degradation in the positioning and navigation solutions (Silva et al., 2013). Yet GNSS space-borne receivers could experience high relative dynamics with respect to the GNSS satellites across different mission phases, handling both large Doppler frequency and Doppler rate, which is its change over time (Chengong et al., 2016).

This work investigates high-sensitivity techniques for GNSS space-borne receivers to enable weak signals acquisition in non-terrestrial applications. The targeted strategies envision coherent acquisition integration time extension to accumulate enough signal energy and cope with low Carrier-to-Noise-density ratio (C/N_0). However, by extending the integration time interval, the Doppler effect on the signal gets emphasized and weakens the acquisition sensitivity improvement ensured by these techniques. In fact, Doppler-shift and Doppler rate impact on acquisition performance by affecting both the carrier and the code layers in the GNSS signal, hence inducing both carrier-Doppler and code-Doppler effects. The former effect generates a shift of the signal carrier frequency, while the latter effect causes a code-chip slipping during the correlation process which translates into an inconsistency between the local code phase and the phase of the incoming signal. In harsh Doppler scenarios, this effect is less problematic if good C/N_0 conditions are met because an excessive integration time extension can be avoided (Nardin et al., 2020, 2021). On the contrary, a key requirement for space-borne GNSS receivers is to have an accurate estimation of the Doppler frequency profile along the mission in order to compensate for it to a certain extent. Based on these premises, this work proposes the use of signal processing algorithms capable to pursue carrier-Doppler and code-Doppler compensation. Such compensation is performed assuming that an estimate of the Doppler profile is provided by a pre-defined Doppler aiding, e.g., through an Orbital Filter (OF) (Capuano et al., 2016). This Doppler aiding is also exploited to centre the Search Space (SS) around the estimated Doppler frequency, thus reducing the number of Doppler frequency bins to be explored. A GNSS software receiver is leveraged for the assessment of both Doppler compensation algorithm and high-sensitivity acquisition techniques suitable for the *snapshot positioning* paradigm for spatial applications. A mission-case scenario is explored about a lunar mission in the framework of the LuGRE payload (Parker et al., 2022). This case study involves an experimental assessment of the performance

of a GNSS receiver to support cis-lunar and lunar navigation, and it foresees a bound on the maximum extension of the coherent acquisition integration time (Minetto et al., 2022). Considering the latter constraint, acquisition performance analysis was carried out in relation to received C/N_0 levels. To this end, three snapshots of the Doppler profile, matching different spacecraft positions along the Moon Transfer Orbit (MTO) were considered.

II. BACKGROUND

Given the discrete-time Intermediate Frequency (IF) samples of the received GNSS signal output by the Radio Frequency (RF) front-end, the acquisition stage attempts to retrieve a rough estimate of satellite synchronisation parameters in terms of code delay τ and Doppler-shift f_D . In conventional GNSS receiver signal processing, this task is accomplished by a bank of correlators which target the Maximum Likelihood (ML) estimation of the vector of parameters $\mathbf{p} = (\tau, f_D)$ for each satellite channel (Kaplan and Hegarty, 2017). Hence, a two-dimensional, discrete correlation function—namely the Cross-Ambiguity Function (CAF)—between the received IF samples $r_{IF}[n]$ and a matched filter w.r.t. a local signal replica is computed over N samples. This operation yields

$$Y(\bar{\tau}, \bar{f}_D) = \frac{1}{N} \sum_{n=0}^{N-1} r_{IF}[n] c[n - \bar{\tau}] e^{j2\pi(f_{IF} + \bar{f}_D)n} \quad (1)$$

where $c[n - \bar{\tau}]$ reproduces a local code with a test delay $\bar{\tau}$ and $e^{j2\pi(f_{IF} + \bar{f}_D)n}$ reproduces a local carrier with a test Doppler frequency shift \bar{f}_D . Since the carrier phase offset is unknown, and is not estimated at this stage, the squared envelope of (1), $S(\bar{\tau}, \bar{f}_D) = |Y(\bar{\tau}, \bar{f}_D)|^2$, is considered to remove the phase dependency. In particular, this envelope is evaluated over a SS grid made of $N_\tau \times N_D$ bins until the CAF maximum is found for some value $\bar{\mathbf{p}} = (\bar{\tau}, \bar{f}_D)$. The time window taken into account for the computation of the CAF is referred to as coherent integration time $T_{coh} = N/f_s$, being $f_s = 1/T_s$ the sampling rate of the Analog-to-Digital Converter (ADC) and T_s the sampling interval. This window is a multiple of the code period T_{code} and, given the periodicity of the incoming code, the correlation peak is expected to fall within one code period.

Concerning the SS grid dimension, the number of delay bins is given by:

$$N_\tau = \frac{T_{code}}{T_s} = T_{code} f_s \quad (2)$$

The longer T_{code} , the larger the number of delay bins. It is worthwhile remarking that (1) is a correlation between the two code replicas; therefore, a code phase offset is indeed estimated rather than the delay of the incoming satellite signal. As regards the Doppler domain, once the Doppler range has been established according to the target application, the number of Doppler frequency bins depends on the choice of the bin size Δf . An empirical rule is usually followed which grants a worst case peak loss below 3 dB:

$$\Delta f = \frac{2}{3T_{coh}} \quad (3)$$

As a matter of fact, the total number of Doppler frequency bins N_D is function of the coherent integration time. A large T_{coh} corresponds to a small Doppler bin, which means more bins to test.

Although multiple schemes exist for the evaluation of the CAF (Kaplan and Hegarty, 2017)—which impact on the Time To First Fix (TTFF) performance of the GNSS receiver—a decision must be taken about whether the satellite is present or not and if it is aligned with the local replica. In such sense, a decision unit synthesizes a set of decision statistics from the SS subset provided by the output of the correlators in each satellite channel (Borio et al., 2008). Since the received IF samples are affected by noise, which is a stochastic component, the values assumed by the CAF in each SS bin can be modelled as random cells X_n with $n = 1, 2, \dots, N_{bin}$ and $N_{bin} = N_\tau N_D$. Then, the Neyman-Pearson (NP) criterion is exploited in order to set a detection threshold B regarding the values of the CAF and, correspondingly, to evaluate the acquisition performance. In particular, NP logic is developed according to two hypothesis:

- H_0 which is verified when the signal is not present or not aligned with the local replica; under this hypothesis, random cells are distributed according to $X_n|H_0 \sim f_{X_n}(\beta)$.
- H_1 which is obtained when the signal is present and correctly aligned; under this hypothesis, random cells are distributed according to $X_n|H_1 \sim f_A(\beta)$.

A detection of the satellite signal in the correct SS bin occurs with probability given by (Borio et al., 2008):

$$P_d(B) = \int_B^{+\infty} f_A(\beta) d\beta \quad (4)$$

However, due to the presence of noise, it can happen that the CAF value of a cell X_n exceeds the threshold in the wrong bin, leading to a false alarm. The *cell false alarm probability* is given by (Borio et al., 2008):

$$P_{fa}(B) = \int_B^{+\infty} f_{X_n}(\beta) d\beta \quad (5)$$

Nevertheless, acquisition performance does not only depend on the statistics characterising each SS cell, but rather threshold-based detection of the CAF maximum evaluated over the whole SS must be taken into account. Therefore, decision statistics are better driven by fixing a target *system false alarm probability* P_{FA} considered in absence of signal. In fact, P_{FA} jointly accounts for both the statistical properties of the SS and the detection strategy adopted (Borio et al., 2008). Then, the cell false alarm probability can be obtained from the system false alarm probability as follows:

$$P_{fa}(B) = 1 - (1 - P_{FA})^{\frac{1}{N_{bin}}} \quad (6)$$

According to (Linatti, 2000), the cell false alarm probability is equal to:

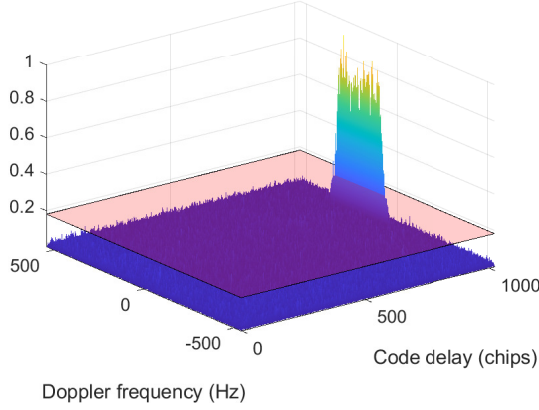
$$P_{fa}(B) = e^{-\frac{B}{2\sigma^2}} \quad (7)$$

where σ^2 is the noise floor variance which is function of the received C/N_0 . Therefore, once P_{fa} is evaluated based on (6), the detection threshold B can be fixed through (7).

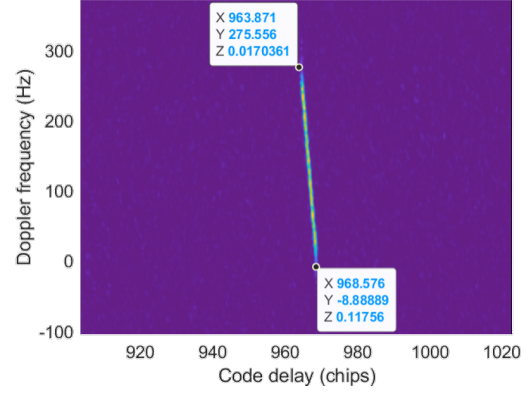
In order to find the maximum value of the CAF, corresponding to the ML estimation of $\mathbf{p} = (\tau, f_D)$, the correlation peak must emerge from the noise floor. The higher and the sharper the peak, the better is the initialization of the tracking stage, leading to better GNSS receiver performance. However, space-borne GNSS receivers are meant to deal with harsh environments where the GNSS signal is subjected to severe distortions and highly attenuated, thus experiencing signal reception at low C/N_0 levels. As such, high sensitivity signal processing techniques are necessary in order to increase the receiver robustness, especially for the acquisition task (Musumeci et al., 2016). Coherent integration time extension is an established approach which increases the number of considered IF samples for the CAF computation by an integer factor M , the latter being the number of coherent sums taken upon correlation. Performing this operation grants an increase of the signal power by a factor proportional to the number of coherent sums. On the contrary, the noise power is constant, as long as Additive White Gaussian Noise (AWGN) assumption is valid (Zekavat and Buehrer, 2011). Hence, the Signal-to-Noise Ratio (SNR) after correlation is increased by a factor of M and the correlation peak is expected to better emerge from the noise floor. By increasing the coherent integration time, the resolution in the Doppler domain is increased as well according to (3). It follows that the time required to evaluate the CAF over the whole SS increases as the number of Doppler bins N_D increases. Therefore, coherent integration time extension enhances receiver sensitivity at the cost of higher processing complexity. Moreover, when the acquired satellite channel is modulated by the navigation message, bit transitions bound the maximum extension of T_{coh} , unless external aiding information is provided about data transitions or dataless (i.e. pilot) channels are employed (Pany et al., 2009).

In order to cope with the pitfalls of pre-detection coherent integration time extension, receiver sensitivity can be enhanced by summing K instances of the CAF envelope. Since the squaring of the CAF removes the phase dependency, envelopes are summed non-coherently (Zekavat and Buehrer, 2011). Performing this accumulation, the signal power increases by a factor proportional to K , while the noise power increases less, by a factor \sqrt{K} . Therefore, non-coherent accumulation allows to increase the separation between correlation peak and noise floor, albeit the squaring loss phenomenon makes the non-coherent accumulation less effective than the coherent extension (Van Diggelen, 2009). As a preferable alternative, the introduction of assistance information via an external aiding can facilitate the acquisition process. In particular, some a-priori knowledge about the expected Doppler frequency shift and Doppler rate can ease weak signal acquisition in space-borne receivers via a reduction of the SS in the Doppler dimension and an extension of the coherent time T_{coh} (Capuano et al., 2016). Moreover, the receiver robustness against high dynamics is enhanced too (Silva et al., 2013).

Unfortunately, by increasing the integration time, the impact of the Doppler frequency shift and the Doppler frequency rate on the carrier frequency and on the code frequency of the acquired satellite channel becomes non negligible. The first effect is known as carrier Doppler, while the latter as the code Doppler. As regards carrier Doppler, it involves a shift of the received carrier frequency with respect to the frequency f_{IF} of the down-converted and digitized signal $r_{IF}[n]$. In particular, the Doppler offset exacerbates in space applications characterised by high-dynamics between the GNSS satellites and the receiver. Even worse, the Doppler frequency continuously changes over time. As a consequence of a non-null Doppler rate, the CAF peak drifts from cell to cell and what comes out from the correlation is a chirp which follows the change of the Doppler frequency. This phenomenon is depicted in Figure 1a, which shows the normalized CAF envelope for a simulated GPS L1 C/A signal acquisition at Medium-Earth Orbit (MEO) altitudes. Considering a fixed Doppler rate R_D and according to (3), the size of the Doppler frequency bin is inversely proportional to the integration time interval. Therefore, the larger T_{coh} , the smaller Δf , and

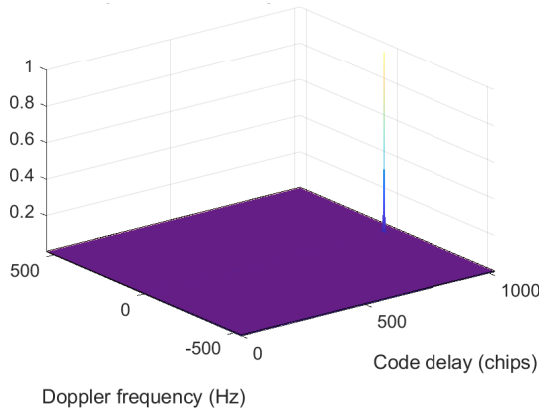


(a) Effect of carrier Doppler (3-D CAF).

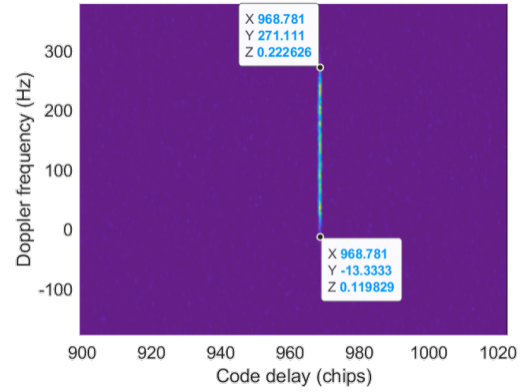


(b) Effect of code Doppler (X-Y plane).

Figure 1: Impact of carrier and code Doppler on the acquisition of GPS L1 C/A code signal with $T_{coh} = 150$ ms. A Doppler frequency rate $R_D = 1800$ Hz/s is considered. Plot of the normalized CAF.



(a) Compensated carrier Doppler (3-D CAF).



(b) Compensated code Doppler (X-Y plane).

Figure 2: Carrier and code Doppler compensation during the acquisition of GPS L1 C/A code signal with $T_{coh} = 150$ ms. A Doppler frequency rate $R_D = 1800$ Hz/s is considered. Plot of the normalized CAF.

the more evident is the drift of the correlation peak. A phenomenon that gets worse for large R_D values as the chirp spans more frequency and code bins. Indeed, the Doppler frequency has an impact on the code frequency as well; when the code Doppler is significant, the spreading code period suffers of a reduction or an expansion. This effect generates a code-chip slipping in the correlation process, producing an inconsistency between the local code phase and the phase of the received signal. As more code periods are used to perform the correlation, the phase slip of the code accumulates producing a strong misalignment between the incoming signal and the local replica. Therefore, if a short integration time is used, the phase slip caused by the code Doppler is negligible. On the contrary, if the acquisition stage requires a longer T_{coh} , like in weak signal environments, the effect of the code Doppler is evident, as shown in Figure 1b. Due to the misalignment, the output power of the correlation is reduced and this leads to a degradation of the acquisition performance, which counterbalance the improvement in sensitivity potentially given by using a longer integration time.

To overcome this problem and to enable a good acquisition of the signal, not only the carrier Doppler shift value, but also its change over time, must be estimated and compensated for. With such a model and exploiting Doppler information provided by external aiding, a Doppler frequency profile can be obtained and de-chirping can be implemented. In practice, the argument used in (1) to perform the carrier wipe-off in the CAF computation must consider a time dependent Doppler profile added to the value of f_D under test. In this way, the Doppler frequency shift and the Doppler rate are both compensated and the chirp is absent in the output of the correlation function, as shown in Fig. 2a. Based on the implemented compensation, the peak is contained in the bin corresponding to the initial value of the Doppler frequency. This is just an implementation choice and it depends on the architecture of the tracking stage. This choice works well if the tracking stage processes the same snapshot of the signal processed by the acquisition. This happens in post-processing conditions and in snapshot positioning implementations. If

instead the tracking exploits the following snapshot of the signal, the acquisition should estimate the last value, in the integration interval, of the Doppler frequency shift. The best implementation choice depends on the receiver and on the application.

Having an estimate of the Doppler frequency profile of the incoming signal, the code Doppler can be derived accordingly and compensated in (1) by forcing the local signal replica $c[n - \bar{\tau}]$ to be dependent on the estimated code Doppler (Foucras et al., 2014). When the compensation of the code Doppler is implemented, the shift of the code delay is absent, as highlighted by Figure 2b, where the CAF presents the effect of the carrier Doppler alone.

III. METHODOLOGY

One of the scientific goals of the LuGRE project is to deeply analyse the signals captured by the GNSS receiver at higher altitudes, on its way to the Moon. For this purpose, the samples of the GNSS signal are collected and then forwarded to ground stations in order to be post-processed, as a scientific support. However, the GNSS payload has a limited storage capability which sets a constraint on the length of the digital GNSS signal that can be stored. Additionally, the downlink window identifies a further limitation. In fact, the GNSS payload must share such window with other scientific payloads involved in the addressed mission. Therefore, it is necessary to limit the bit rate for the transmission of the recorded GNSS signal samples to the ground stations and, correspondingly, the length of the recorded signal chunk is constrained as well. Hence, this work foresees a technical limit on the length of the signal and, consequently, a bound on the extension of the integration time.

In light of the foregoing, a 150 ms bound has been set to the extension of overall integration time for the tests carried out in this study. This constraint has been considered as a target when analyzing the acquisition performance of the receiver. Such a limit also suffices to save and transmit, with the available resources, GNSS samples for ground post-processing to allow a complementary analysis of the behavior of GNSS receivers for space applications.

Given the addressed scenario, some analyses have been carried out about the performance of a high sensitivity GNSS receiver. Specifically, requirements about the extension of T_{coh} have been examined for different C/N_0 levels, establishing compliance with the mission technical bounds. Additionally, it has been investigated how to improve the performance by changing the system and cell false alarm probability, P_{FA} and P_{fa} , and reducing the number of Doppler frequency bins N_D in the acquisition stage. Throughout these experiments, it has been assumed the availability of an estimation of the Doppler frequency profile via an external aiding in order to allow for the compensation of the Doppler shift and the Doppler rate both on the carrier and on the code, as described in Section II.

In view of these considerations, the performance of the acquisition stage, exploiting high sensitivity strategies, has been tested. In particular, coherent and non-coherent accumulation techniques have been used. Signals received with different C/N_0 levels have been considered, corresponding to the different distances within the cis-lunar space. To do so, it has been exploited a mission-related path-loss model approximating the experienced C/N_0 profile with respect to the distance from the Earth's centre. Specifically, the addressed scenario focuses on distances greater than those of the MEO orbits of the GNSS satellites. Hence, the model applies to these distances and C/N_0 values concerning distances smaller than the MEO orbits must not be taken into account. Fig. 3 shows the plot of the C/N_0 profile, given a generalized preliminary model. The MEO region, where GNSS satellites are located, is highlighted as well as the distance of the Moon from the Earth. Obviously, the higher the distance from the Earth, the lower the C/N_0 values. The worst case scenario is at a distance of 60 radius earth (RE), i.e. Earth-Moon distance, where the C/N_0 is about 18 dB-Hz.

1. Parametric analysis scenario

In order to test the acquisition performance of the software receiver, a dataless GPS L1 signal (PRN 1) has been generated for each C/N_0 level of Fig. 3 fixing a constant Doppler rate equal to 5 Hz/s. The analysis results are reported in Section IV.1. After setting $P_{FA} = 10^{-3}$, three different SS sizes have been taken into account, corresponding to three different number of Doppler frequency bins: $N_D = 3$, $N_D = 5$ and $N_D = 243$. In particular, N_D can be reduced to few bins if a sufficiently accurate external aiding is provided to the receiver. In fact, besides being used to implement the Doppler compensation, the Doppler profile information can be used to center the SS around the initial value of f_D . By changing N_D , and thus the SS size, the value of T_{coh} necessary to acquire signals changes too. This is due to the fact that the acquisition threshold B is fixed according to (7). Since there are less bins, the same P_{FA} can be obtained with a lower threshold, which is generally exceeded for a shorter T_{coh} . Initially, signals have been processed exploiting only coherent accumulation. In that way, it has been possible to define, for each N_D , the requirements in terms of length of the coherent integration interval. The experiments have been then repeated for a combination of coherent and non-coherent sums.

Besides varying N_D , P_{FA} can be changed to find a proper value which allows to use a smaller T_{coh} , but maintaining a good acquisition accuracy. Another possible solution, is to directly fix the cell false alarm probability P_{fa} to a specific value, instead of deriving it from the system false alarm probability P_{FA} . The larger this parameter is set, the smaller the threshold will be and the smaller T_{coh} needed for the acquisition. Several tests have been made in both cases, to understand which are reasonable

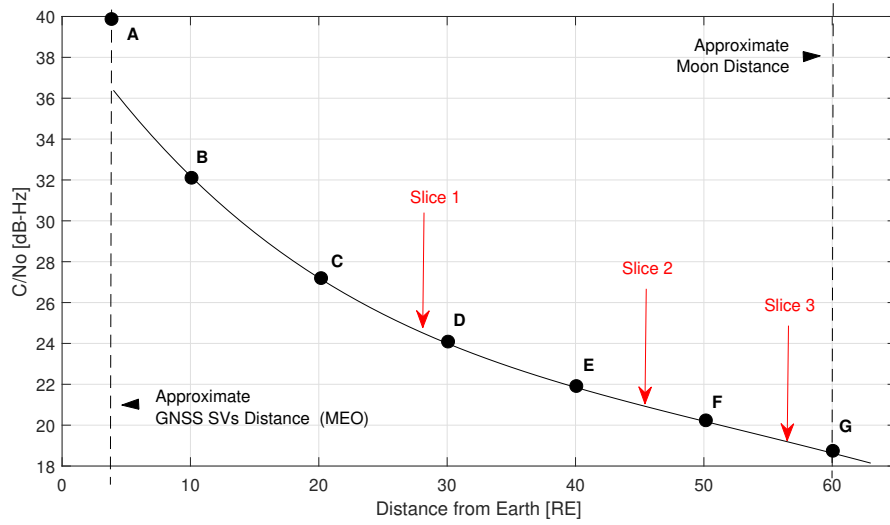


Figure 3: Approximate model of C/N_0 for distances included in the cis-lunar space. Black dots show sampling of C/N_0 along the distance used in the parametric analysis while red arrows indicate the C/N_0 assumed for the slicing of the trajectory in the simulated MTO experiment. MEO GNSS orbits and Moon distance are highlighted as reference.

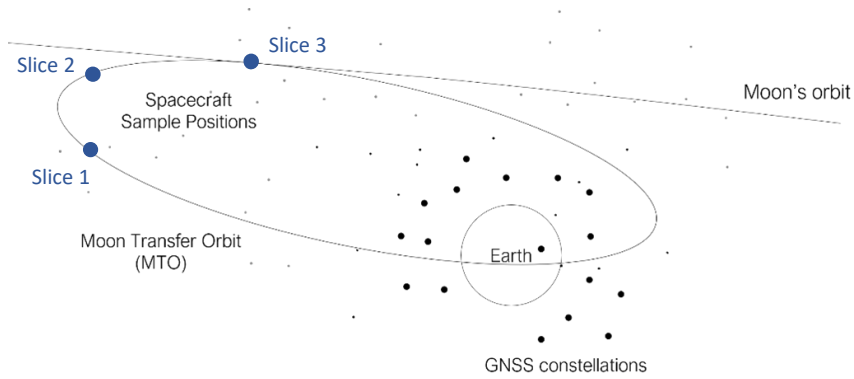


Figure 4: Pictorial view of spacecraft's sample locations along the simulated Moon Transfer Orbit (MTO).

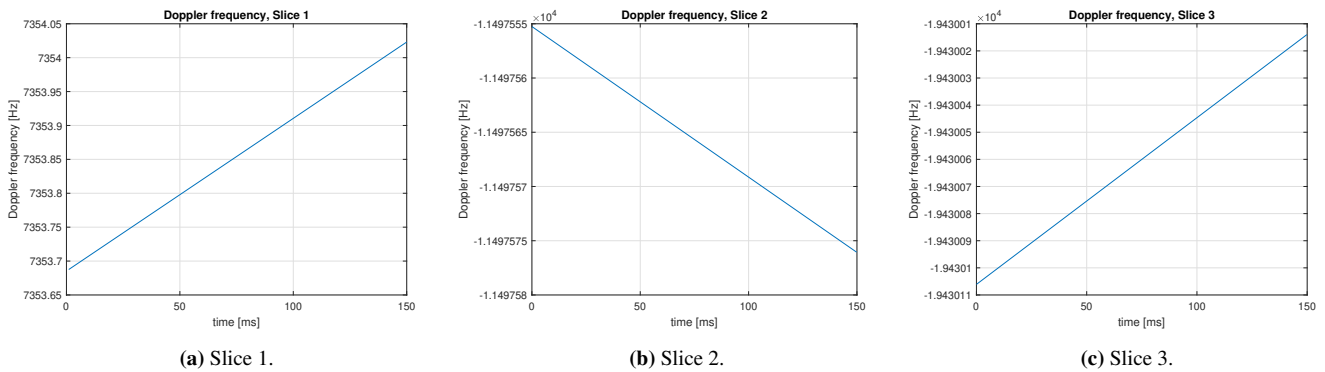


Figure 5: Doppler frequency profiles at different time windows along the MTO.

values for these parameters.

2. Simulated MTO scenario

A more realistic scenario is investigated in Section IV.2. Three slices of the Doppler profile experienced by a spacecraft on a sample MTO, with respect to the GPS satellite transmitting the Pseudo Random Noise (PRN) 1, have been extracted through AGI Systems Tool Kit (STK). Figure 4 shows the spacecraft location on the MTO for slice 1, slice 2 and slice 3. Figures 5 shows the three Doppler profiles, related to GNSS signal chunks of 150 ms. In these short intervals, all the Doppler profiles are assumed to follow a linear trend in time. These slices are associated to different positions of the spacecraft on the MTO at different times, and the spacecraft can either approach the transmitting satellite or move away from it. In fact, for slices 1 and 3 the Doppler shift increases, while for slice 2 it decreases. Three GPS L1 signals (PRN 1), characterized by these Doppler curves, have been generated and then processed by the software receiver, which leveraged on the three profiles as Doppler aiding for the acquisition engine.

Slice 1 is related to the time window in which the spacecraft is at a distance of about 28.67 RE from the Earth. Given so, the corresponding received C/N_0 level has been obtained through the model of Fig. 3, and it amounts to about 24.35 dB-Hz. The initial Doppler frequency, corresponding to the first sample of the Doppler profile, is 7353.69 Hz, and the Doppler rate is about 2.25 Hz/s. Among the analysed Doppler profiles, slice 1 is related to the time frame in which the spacecraft is closest to the GNSS constellation. In fact, it is characterized by a Doppler rate which is higher than those measured for the other slices. Accordingly, the corresponding C/N_0 level is the highest among the considered slices.

Slice 2, instead, is characterized by a distance from the Earth of about 39.84 RE, with an associated C/N_0 level of 21.88 dB-Hz. The initial Doppler frequency is -11497.55 Hz, while the Doppler rate is -0.14 Hz/s.

Finally, slice 3 relates to the instant in which the spacecraft is at a distance of 58.61 RE from the Earth, which is almost the Earth-Moon distance. In fact, this slice is characterized by a low C/N_0 level equal to 18.86 dB-Hz. In this case the initial frequency of the Doppler profile measures -19430.11 Hz and varies with a rate of 0.61 Hz/s. As in the previous analysis, the minimum T_{coh} necessary to acquire the GNSS signals received in correspondence of three slices of Doppler profile has been investigated, setting a target $P_{FA} = 10^{-3}$ and exploiting coherent sums only.

IV. RESULTS

1. Parametric analysis results

a) Parametric analysis in relation to the size of the search space

A first experimental campaign aimed at assessing the acquisition performance depending on the size of the SS. Given N_D Doppler bins in the SS, the length of the coherent integration time necessary to acquire the signals, for each value of N_D and for different C/N_0 levels, is reported in Table 1. The smaller the C/N_0 , the larger must be the coherent integration time T_{coh} to be able to acquire the satellite. By setting a smaller N_D , which means reducing the SS size, the value of T_{coh} necessary to acquire signals is reduced too, because the same P_{FA} is obtained with a lower threshold B , as explained in Section II. The bound on the overall integration time considered in this analysis is 150 ms. Fixing $P_{FA} = 10^{-3}$ and taking into account the limitation on T_{coh} , the acquisition of the signal is possible down to $C/N_0 = 21.852$ dB-Hz. This value corresponds to a distance of 40 RE, which is almost 70% of the Earth-Moon distance. However, to acquire signals at the Moon distance with the current scenario, more samples of the signals must be processed, to exploit a higher T_{coh} .

Table 1: Coherent sums: analysis of T_{coh} needed for the acquisition for different values of C/N_0 and with different N_D . System false alarm probability fixed to $P_{FA} = 10^{-3}$.

| C/N_0 | C/N_0 | T_{coh} [ms] | T_{coh} [ms] | T_{coh} [ms] |
|-------------|---------|----------------|----------------|----------------|
| Scenario ID | [dB-Hz] | $N_D = 3$ | $N_D = 5$ | $N_D = 243$ |
| A | 39.821 | 2 | 2 | 2 |
| B | 32.191 | 6 | 7 | 8 |
| C | 27.211 | 41 | 43 | 60 |
| D | 24.004 | 89 | 89 | 121 |
| E | 21.852 | 100 | 100 | 107 |
| F | 20.197 | 157 | 158 | 175 |
| G | 18.634 | 228 | 368 | 418 |

In Table 2, the results about acquisition using the combination of coherent and non-coherent accumulations are shown. In particular, the length of T_{coh} and the number of non-coherent sums K are reported. In all cases, the overall integration time required to acquire the signal ($K \cdot T_{coh}$) is generally higher with respect to the case in which only coherent sums are employed. Exploiting non-coherent accumulations is not beneficial in terms of required signal length to be processed. Moreover, the performance gain is limited by the squaring loss (Van Diggelen, 2009). However, non-coherent accumulations are useful when

data-bit transitions are present.

Both using coherent accumulation alone and combined with non-coherent one, having a bounded integration interval with maximum length of 150 ms is not sufficient to acquire signals with $C/N_0 = 20.197$ dB-Hz, and $C/N_0 = 18.634$ dB-Hz, even using less Doppler frequency bins. Therefore, in order to reach these levels, besides N_D , it is necessary to tune P_{fa} and P_{FA} parameters too.

Table 2: Combination of coherent and non-coherent sums: analysis of T_{coh} and K needed for the acquisition for different values of C/N_0 and with different N_D . System false alarm probability fixed to $P_{FA} = 10^{-3}$.

| C/N_0 Scenario ID | C/N0 [dB-Hz] | T_{coh} [ms] $N_D = 3$ | T_{coh} [ms] $N_D = 5$ | T_{coh} [ms] $N_D = 243$ |
|------------------------|-----------------|-----------------------------|-----------------------------|-------------------------------|
| A | 39.821 | 1 (K=2) | 1 (K=2) | 1 (K=2) |
| B | 32.191 | 4 (K=2) | 4 (K=2) | 5 (K=2) |
| C | 27.211 | 15 (K=3) | 15 (K=3) | 15 (K=4) |
| D | 24.004 | 39 (K=3) | 40 (K=3) | 43 (K=3) |
| E | 21.852 | 26 (K=4) | 27 (K=4) | 30 (K=4) |
| F | 20.197 | 33 (K=5) | 33 (K=5) | 35 (K=6) |
| G | 18.634 | 150 (K=3) | 226 (K=2) | 300 (K=2) |

b) Parametric analysis in relation to false alarm probability

The analysis has been carried on by investigating the performance with respect to the cell false alarm probability P_{fa} and the system false alarm probability P_{FA} . Table 3 shows the required T_{coh} to acquire signals with different C/N_0 levels and P_{FA} , fixing $N_D = 3$. Increasing the system false alarm probability from 10^{-2} to 10^{-2} and 10^{-3} allows to acquire signals with a smaller integration time. With these larger values of P_{FA} , it has been possible to acquire with $T_{coh} \leq 150$ ms even a sample signal with $C/N_0 = 20.197$ dB-Hz.

Table 3: Coherent sums: analysis of T_{coh} needed for the acquisition for different values of C/N_0 , with $N_D = 3$. System false alarm probability P_{FA} fixed to different values.

| C/N_0 Scenario ID | C/N0 [dB-Hz] | T_{coh} [ms] $P_{FA} = 10^{-1}$ | T_{coh} [ms] $P_{FA} = 10^{-2}$ | T_{coh} [ms] $P_{FA} = 10^{-3}$ |
|------------------------|-----------------|--------------------------------------|--------------------------------------|--------------------------------------|
| A | 39.821 | 1 | 1 | 2 |
| B | 32.191 | 5 | 6 | 6 |
| C | 27.211 | 34 | 40 | 41 |
| D | 24.004 | 63 | 72 | 89 |
| E | 21.852 | 83 | 88 | 100 |
| F | 20.197 | 64 | 72 | 157 |
| G | 18.634 | 201 | 217 | 228 |

The same analysis has been carried out by fixing the cell false alarm probability P_{fa} , instead of the system false alarm probability. Results are shown in Table 4. Also in this case, T_{coh} needed for the acquisition is smaller than the values reported in Table 1. Both P_{fa} and P_{FA} parameters can be fixed depending on the requirements and can improve the minimum T_{coh} at the cost of a higher chance of false alarm. In fact, the higher these parameters are set, the more probable is to have a cell exceeding the threshold in a wrong bin. Hence, it could be a valid strategy to face a constraint on T_{coh} .

2. Simulated MTO results

A final realistic scenario has been addressed and the results are reported in this section. As in the previous section, we analysed the length of T_{coh} required for acquiring the signals, here related to three slices of Doppler profile. When the system false alarm probability is fixed to 10^{-3} and only coherent sums are exploited, it is possible to acquire the GPS satellite with $T_{coh} \leq 150$ ms only for the slice 1 (Table 5).

For slice 2 just over 150 ms are needed, when $N_D = 3$ and $N_D = 5$. When instead $N_D = 243$ bins are used, the length of the coherent integration time needed for the acquisition is $T_{coh} = 179$ ms. As for slice 3, T_{coh} is much larger than the bound. Using both coherent and non-coherent sums (Table 6), the integration time results are similar to those of the previous section, meaning that the combination of these techniques does not allow to obtain a smaller overall integration interval. Also in this case, there is some margin for improvement by exploiting cell and system false alarm probabilities.

Table 4: Coherent sums: analysis of T_{coh} needed for the acquisition for different values of C/N_0 , with $N_D = 3$. Single cell false alarm probability P_{fa} fixed to different values.

| Scenario ID | C/N_0 [dB-Hz] | T_{coh} [ms] $P_{fa} = 10^{-6}$ | T_{coh} [ms] $P_{fa} = 10^{-7}$ | T_{coh} [ms] $P_{fa} = 10^{-8}$ |
|-------------|-----------------|---|---|---|
| A | 39.821 | 1 | 1 | 1 |
| B | 32.191 | 5 | 6 | 6 |
| C | 27.211 | 34 | 40 | 41 |
| D | 24.004 | 65 | 71 | 88 |
| E | 21.852 | 79 | 88 | 97 |
| F | 20.197 | 63 | 71 | 157 |
| G | 18.634 | 201 | 212 | 225 |

Table 5: Coherent sums: analysis of T_{coh} needed for the acquisition for the 3 slices, with different N_D . System false alarm probability fixed to $P_{FA} = 10^{-3}$.

| Slice | C/N_0 [dB-Hz] | T_{coh} [ms] $N_D = 3$ | T_{coh} [ms] $N_D = 5$ | T_{coh} [ms] $N_D = 243$ |
|-------|-----------------|------------------------------------|------------------------------------|--------------------------------------|
| 1 | 24.35 | 70 | 70 | 74 |
| 2 | 21.88 | 155 | 156 | 179 |
| 3 | 18.86 | 249 | 271 | 334 |

By setting P_{FA} to 10^{-2} and 10^{-1} it has been possible to acquire the GPS signal, corresponding to slice 2, with an integration time smaller than 150 ms (Table 7). The same happened fixing P_{fa} to 10^{-7} and 10^{-6} , as it can be seen in Table 8. Instead, signal associated to slice 3 requires a $T_{\text{coh}} > 150$ ms even with larger values of P_{FA} and P_{fa} . Also for this signal the required T_{coh} is reduced when larger P_{FA} or P_{fa} are used.

3. Maximum acceptable offset for the Doppler aiding

It has been shown that, in order to be able to compensate the Doppler frequency and Doppler frequency rate, an accurate estimate of the Doppler profile must be provided to the acquisition stage. It is thus important to understand the effect on the acquisition when an error on the Doppler profile aiding is present. In particular, the consequences of an offset which causes a misalignment in time of the estimated Doppler profile with respect to the correspondent snapshot of the signal have been analyzed. If the Doppler frequency changes linearly in time, or almost linearly, even if there is an offset the compensation of Doppler rate presented in Section II still works. Indeed, if the Doppler rate is almost constant, the misalignment is always the same. Hence, it is sufficient that the provided Doppler rate is correct. However, the estimation of the Doppler frequency is fundamental to reduce the number of Doppler frequency bins as well. In fact, the SS is centred around the initial value of the Doppler profile and the number of bins is reduced. Depending on the number of Doppler frequency bins N_D to be tested and on the length of the integration interval T_{coh} , there is a different level of robustness against the frequency aiding error. T_{coh} together with N_D , should be decided depending on the accuracy of the Orbital Filter. The more accurate is the Doppler frequency estimation, the smaller can be N_D . In general, the maximum acceptable error, so the maximum acceptable shift of the SS centre from the correct value, depends on the number of Doppler frequency bins to be tested and it is equal to:

$$\text{MS}_{[bin]} = \frac{N_D - 1}{2} \quad (8)$$

In case of constant Doppler rate R_D and supposing that the Doppler profile, provided by the Orbital Filter, is subjected to a misalignment of $S_{[s]}$ seconds, the correspondent shift in frequency is:

$$S_{[Hz]} = R_D \cdot S_{[s]} \quad (9)$$

While, the respective shift in number of bins is then:

$$S_{[bin]} = \frac{S_{[Hz]}}{\Delta f} \quad (10)$$

Table 6: Combination of coherent and non-coherent sums: analysis of T_{coh} and K needed for the acquisition for the 3 slices, with different N_D . System false alarm probability fixed to $P_{FA} = 10^{-3}$.

| Slice | C/N0 [dB-Hz] | T_{coh} [ms] | T_{coh} [ms] | T_{coh} [ms] |
|-------|-----------------|----------------|----------------|----------------|
| | | $N_D = 3$ | $N_D = 5$ | $N_D = 243$ |
| 1 | 24.35 | 25 (K=3) | 27 (K=3) | 51 (K=2) |
| 2 | 21.88 | 107 (K=2) | 109 (K=2) | 182 (K=2) |
| 3 | 18.86 | 183 (K=2) | 183 (K=2) | 190 (K=2) |

Table 7: Coherent sums: analysis of T_{coh} needed for the acquisition for the 3 slices, with $N_D = 3$. System false alarm probability P_{FA} fixed to different values.

| Slice | C/N0 [dB-Hz] | T_{coh} [ms] | T_{coh} [ms] | T_{coh} [ms] |
|-------|-----------------|--------------------|--------------------|--------------------|
| | | $P_{FA} = 10^{-1}$ | $P_{FA} = 10^{-2}$ | $P_{FA} = 10^{-3}$ |
| 1 | 24.35 | 63 | 67 | 70 |
| 2 | 21.88 | 109 | 121 | 155 |
| 3 | 18.86 | 199 | 221 | 249 |

In the previous analyses, a bound on the extension of T_{coh} has been considered. Having a limited integration interval, allows to define the maximum acceptable offset. As an example, let's consider the Doppler profile of Slice 1 in Section III.2, whose Doppler rate is about $R_D = 2.25$ Hz/s. If T_{coh} is fixed to 150 ms, following the empirical rule (3), the Doppler frequency bin size Δf is fixed too, and it is about 4.44 Hz. Based on the accuracy of the Orbital Filter and on N_D , different situations could happen. Supposing an offset on the Doppler profile of about $S_{[s]} \simeq 7$ s, the respective shift in frequency is $S_{[Hz]} \simeq 15.75$ Hz. Due to this error, the SS is centred around the wrong value, which is the shifted one. Indeed, the peak in the CAF is not placed in centre of the SS, it is instead shifted of 3 bins. Depending on the value of N_D , different scenarios occur. As an example, we addressed those investigated so far:

- $N_D = 243$: since the SS is quite large, even if the correct value of f_D shifts 3 bins away from the centre of the SS, it is still possible to find the peak and to acquire the satellite. Indeed, as shown in Fig. 6a, the peak is found at $\bar{f}_D = -13.33$ Hz. In fact, from (10), the shift in frequency from the right bin is $S_{[Hz]} = S_{[bin]} \cdot \Delta f = 3 \cdot 4.44$ Hz = 13.33 Hz.
- $N_D = 5$: the Doppler frequency range of the CAF is too small to contain the peak shifted from the centre due to the offset. In fact, it goes from -8.89 Hz to 8.89 Hz. Therefore, it is not possible to find a peak above threshold and the satellite is not acquired (Fig. 6b). According to (8), in order to be able to acquire the satellite, the shift caused by the error should be less or equal than $MS_{[bin]} = 2$ bins. Fig. 6c shows the plot of 2-D CAF in the Doppler frequency domain in case a shift of 2 bins is caused by the frequency aiding error. The peak is in the first bin, corresponding to -8.89 Hz, and the satellite is correctly acquired.
- $N_D = 3$: as for $N_D = 5$, with an offset of 3 bins, it is not possible to acquire the satellite. In this case, the CAF is characterized by a Doppler frequency domain going from -4.44 Hz to 4.44 Hz (Fig. 6d). For $N_D = 3$, the maximum acceptable shift is only of 1 bin (8). Indeed, when the error of the Doppler profile estimate causes the shift of 1 bin, the peak is still present and the satellite can be acquired (Fig. 6e).

Since T_{coh} is fixed to 150 ms and the Doppler rate is almost constant, for each value of N_D it is possible to define the maximum shift in frequency and in time, starting from (8). For example, when $N_D = 5$, $MS_{[bin]}$ is 2 bins. Therefore, from (10), $S_{[Hz]} = 8.89$ Hz. Actually, all values up to about $f_D = 8.89 + \frac{\Delta f}{2}$ Hz will fall in that last bin. Therefore, the maximum offset in frequency is $MS_{[Hz]} = 11.11$ Hz. Instead, from (9), the maximum misalignment in time is $MS_{[s]} = MS_{[Hz]}/R_D \simeq 5$ s. Anyway, this is a particular case, with a specific constraint on T_{coh} , but in general, the maximum shift in frequency and time depends on:

- The length of the coherent integration time T_{coh} : if the empirical rule (3) is used, T_{coh} determines the size of the Doppler frequency bins. In particular, the larger T_{coh} , the smaller the Doppler frequency bin size. Therefore, it is even more risky employing a small value of N_D , because it is more probable that the peak shifts out of range.
- The Doppler rate: given a misalignment in time, the larger the Doppler rate, the larger the shift of the peak, the smaller should be the error.

Besides the accuracy of the Orbital Filter, a shift is caused by the clock drift of the receiver. The clock is not perfectly stable, and its drift causes an additional shift. Therefore, the total offset, which corresponds to the total shift from the right bin, is given

Table 8: Coherent sums: analysis of T_{coh} needed for the acquisition for the 3 slices, with $N_D = 3$. System false alarm probability P_{FA} fixed to different values.

| Slice | C/N0 [dB-Hz] | T_{coh} [ms] $P_{\text{FA}} = 10^{-6}$ | T_{coh} [ms] $P_{\text{FA}} = 10^{-7}$ | T_{coh} [ms] $P_{\text{FA}} = 10^{-8}$ |
|-------|-----------------|--|--|--|
| 1 | 24.35 | 62 | 66 | 70 |
| 2 | 21.88 | 105 | 121 | 154 |
| 3 | 18.86 | 195 | 208 | 247 |

by the error due to the Doppler aiding and the drift of the clock. The sum of these components must be within the maximum acceptable error and this should be taken into account when setting N_D .

To sum up, employing a smaller N_D allows to reduce the T_{coh} needed for the acquisition. The smaller N_D , the faster is the acquisition and the less processing and memory is required. However, the smaller is the acceptable error offset related to the Doppler profile estimate provided by the Orbital Filter. Therefore, a trade-off must be found between the performance of the acquisition and the computational effort of the GNSS receiver.

V. CONCLUSIONS

Results about the studied scenario highlight the need for longer coherent integration times in acquisition than those typically employed for terrestrial applications. Coherent integration turns out to be more effective than non-coherent accumulation, because of the squaring loss phenomenon the latter method is subjected to. Nevertheless, coherent integration time extension translates into the need for pilot channels (to avoid bit transitions), lower bitrates than those currently used for the transmission of GNSS navigation messages, or external aiding for data removal. Moreover, longer integration times require the compensation of accumulated Doppler shift, to allow both an effective acquisition process and a correct tracking loop initialisation. Given the aforementioned limitations, this study also addressed a way to improve acquisition performance in terms of minimum required coherent integration time. It turned out that, by reducing and setting the proper values of cell and system false alarm probability (respectively, P_{fa} and P_{FA}) allows to get signals with a smaller coherent integration time T_{coh} . These analyses have also confirmed the fundamental importance of an accurate Doppler aiding information by a Doppler aiding stage for an effective reduction of the SS, another factor that diminish the need for large T_{coh} values. Based on the presented conditions and the adopted models, the acquisition of GNSS signals is possible in the cis-lunar space and on the lunar surface. To complete the prototyping of the Lunar GNSS software receiver, further analysis of the tracking stage is needed to confirm the overall effectiveness of the acquisition strategies implemented and analysed in this study. Future works can analyse the feasibility of dynamically setting the number of Doppler frequency bins, and the length of the integration time depending on the uncertainty of the Doppler aiding.

ACKNOWLEDGEMENTS

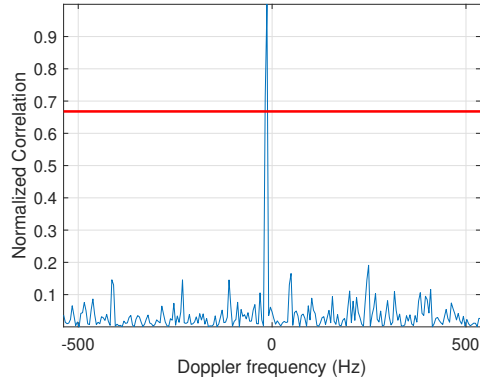
This study was funded within the contract n. 2021-26- HH.0 ASI/Politecnico di Torino "Attività di R&S inerente alla Navigazione GNSS nello Space volume Terra/Luna nell'ambito del Lunar GNSS Receiver Experiment".

REFERENCES

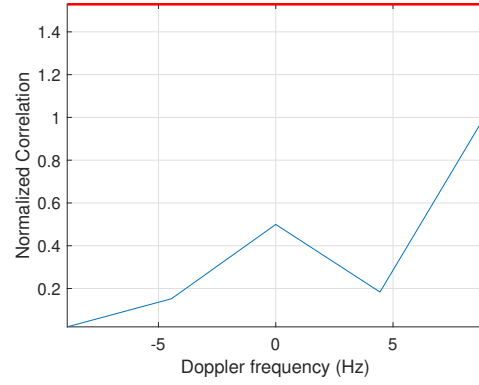
- Amir, A.-Z., El-Mowafy, A., et al. (2021). Precise orbit determination of LEO satellites based on undifferenced GNSS observations. *Journal of surveying engineering*, 18(1):1–22.
- Borio, D., Camoriano, L., and Lo Presti, L. (2008). Impact of gps acquisition strategy on decision probabilities. *IEEE Transactions on Aerospace and Electronic Systems*, 44(3):996–1011.
- Burch, J., Moore, T., Torbert, R., and Giles, B. (2016). Magnetospheric multiscale overview and science objectives. *Space Science Reviews*, 199(1):5–21.
- Capuano, V., Basile, F., Botteron, C., and Farine, P.-A. (2016). GNSS-based orbital filter for Earth Moon Transfer Orbits. *The Journal of Navigation*, 69(4):745–764.
- Capuano, V., Botteron, C., Leclère, J., Tian, J., Wang, Y., and Farine, P.-A. (2015). Feasibility study of GNSS as navigation system to reach the Moon. *Acta Astronautica*, 116:186–201.
- Chengong, Z., Xi, C., and Zhen, H. (2016). A comprehensive analysis on Doppler frequency and Doppler frequency rate characterization for GNSS receivers. In *2016 2nd IEEE International Conference on Computer and Communications (ICCC)*,

- pages 2606–2610. IEEE.
- Delépaut, A., Minetto, A., Dovis, F., Melman, F., Giordano, P., and Ventura-Traveset, J. (2022). Enhanced GNSS-based positioning in space exploiting inter-spacecraft cooperation. In *Proceedings of the 2022 International Technical Meeting of The Institute of Navigation*, pages 530–544.
- Farahmand, M., Long, A., and Carpenter, R. (2015). Magnetospheric multiscale mission navigation performance using the goddard enhanced onboard navigation system. In *Proceedings of the 25th International Symposium on Space Flight Dynamics*, pages 19–23.
- Foucras, M., Julien, O., Macabiau, C., and Ekambi, B. (2014). Detailed analysis of the impact of the code doppler on the acquisition performance of new gnss signals. In *Proceedings of the 2014 International Technical Meeting of the Satellite Division of The Institute of Navigation*, pages 513–524.
- Gill, E., Montenbruck, O., and Kayal, H. (2001). The BIRD Satellite Mission as a Milestone Toward GPS-based Autonomous Navigation. *Navigation*, 48(2):69–75.
- Hartrampf, M., Filippi, H., Krauss, P. A., Montenbruck, O., and Gottzein, E. (2015). LION navigator for transfer to GEO using electric propulsion. In *Proceedings of the 28th International Technical Meeting of the Satellite Division of The Institute of Navigation (ION GNSS+ 2015)*, pages 3910–3927.
- Innati, J. (2000). On the threshold setting principles in code acquisition of DS-SS signals. *IEEE Journal on Selected Areas in Communications*, 18(1):62–72.
- ISECG, I. S. E. C. G. (2018). The Global Exploration Roadmap. Technical report, International Space Exploration Coordination Group (ISECG).
- Kaplan, E. D. and Hegarty, C. (2017). *Understanding GPS/GNSS: principles and applications*. Artech house.
- Lannes, C. (2011). A new Generation of Monitoring and Control System for ESTRACK. In *SpaceOps 2012 conference*.
- Miller, J. J. (2018). International Committee on GNSS-13 Focuses on PNT in High Earth Orbit and Beyond.
- Minetto, A., Dovis, F., Nardin, A., Vouch, O., Impresario, G., and Musmeci, M. (2022). Analysis of GNSS data at the Moon for the LuGRE project. In *2022 IEEE International Workshop on Metrology for AeroSpace (MetroAeroSpace)*.
- Montenbruck, O., Markgraf, M., Garcia-Fernandez, M., and Helm, A. (2008). GPS for microsattelites–status and perspectives. In *Small satellites for earth observation*, pages 165–174. Springer.
- Musumeci, L., Dovis, F., Silva, J. S., da Silva, P. F., and Lopes, H. D. (2016). Design of a High Sensitivity GNSS receiver for Lunar missions. *Advances in Space Research*, 57(11):2285–2313.
- Nardin, A., Dovis, F., and Fraire, J. A. (2020). Empowering the tracking performance of LEO PNT by means of meta-signals. In *2020 IEEE International Conference on Wireless for Space and Extreme Environments (WiSEE)*, pages 153–158.
- Nardin, A., Dovis, F., and Fraire, J. A. (2021). Empowering the tracking performance of LEO-based positioning by means of meta-signals. *IEEE Journal of Radio Frequency Identification*, 5(3):244–253.
- Pany, T., Riedl, B., Winkel, J., Woerz, T., Schweikert, R., Niedermeier, H., Lagrasta, S., Lopez-Risueno, G., and Jiménez-Baños, D. (2009). Coherent integration time: The longer, the better. *Inside GNSS*, 4:52–61.
- Parker, J., Bauer, F., Ashman, B., Miller, J., Enderle, W., and Blonski, D. (2018). Development of an Interoperable GNSS Space Service Volume. In *Proceedings of the 31st International Technical Meeting of the Satellite Division of The Institute of Navigation (ION GNSS+ 2018)*, Miami, Florida, pages 1246–1256.
- Parker, J. J., Dovis, F., Anderson, B., Ansalone, L., Ashman, B., Bauer, F. H., D’Amore, G., Facchinetti, C., Fantinato, S., Impresario, G., et al. (2022). The Lunar GNSS Receiver Experiment (LuGRE). In *Proceedings of the 2022 International Technical Meeting of The Institute of Navigation*, pages 420–437.
- Rush, J. (2000). Current issues in the use of the global positioning system aboard satellites. *Acta Astronautica*, 47(2-9):377–387.
- Silva, P. F., Lopes, H. D., Peres, T., Silva, J., Ospina, J., Cichocki, F., Dovis, F., Musumeci, L., Serant, D., Calmettes, T., et al. (2013). Weak GNSS signal navigation to the moon. In *Proceedings of the 26th International Technical Meeting of the Satellite Division of The Institute of Navigation (ION GNSS+ 2013)*, pages 3357–3367.
- Teunissen, P. J. and Montenbruck, O. (2017). *Springer handbook of global navigation satellite systems*, volume 10. Springer.
- United Nations (UN) (2018). *The interoperable global navigation satellite systems space service volume*. U.N.

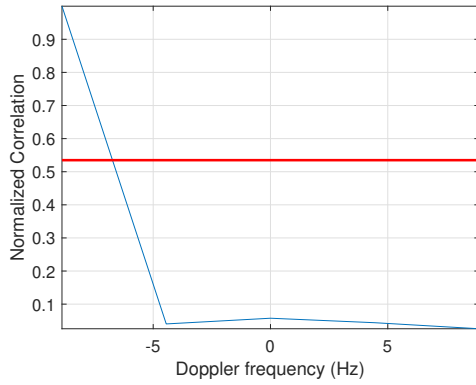
- Van Diggelen, F. S. T. (2009). *A-GPS: assisted GPS, GNSS, and SBAS*. Artech house.
- Vetter, J. R. (2007). Fifty Years of Orbit Determination: Development of Modern Astrodynamics Methods. *Johns Hopkins APL technical digest*, 27(3):239.
- Winternitz, L. M., Bamford, W. A., and Heckler, G. W. (2009). A gps receiver for high-altitude satellite navigation. *IEEE Journal of Selected Topics in Signal Processing*, 3(4):541–556.
- Zekavat, R. and Buehrer, R. M. (2011). *Handbook of position location: Theory, practice and advances*, volume 27. John Wiley & Sons.



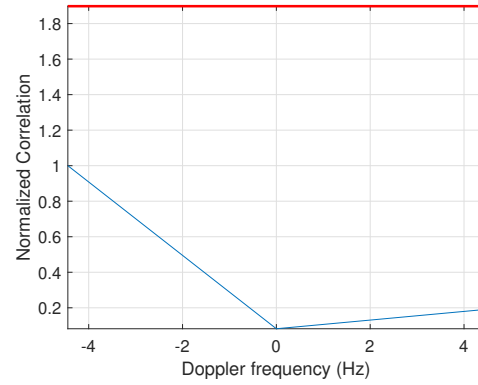
(a) Shift of 3 bins from the right \bar{f}_D , by assuming $N_D = 243$.



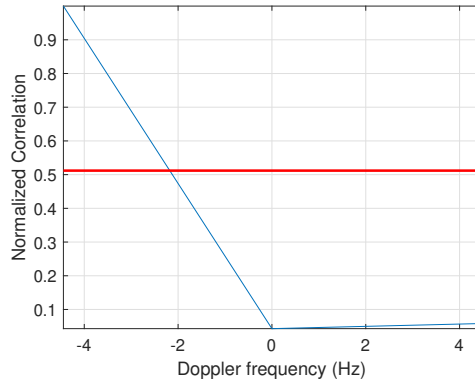
(b) Shift of 3 bins from the right \bar{f}_D , by assuming $N_D = 5$.



(c) Shift of 2 bins from the right \bar{f}_D , by assuming $N_D = 5$.



(d) Shift of 3 bins from the right \bar{f}_D , by assuming $N_D = 3$.



(e) Shift of 1 bins from the right \bar{f}_D , by assuming $N_D = 3$.

Figure 6: Acquisition of a GPS L1 C/A signal with $T_{coh} = 150$ ms in presence of a shift of the peak, due to an error of the frequency aiding.